International Journal of Plasticity 64 (2015) 177–192

Contents lists available at ScienceDirect

International Journal of Plasticity

journal homepage: www.elsevier.com/locate/ijplas

Investigation using digital image correlation of Portevin-Le Chatelier Effect in Hastelloy X under thermo-mechanical loading

B. Swaminathan [a,1], W. Abuzaid [b,2], H. Sehitoglu [b], J. Lambros [a,*]

[a] Aerospace Engineering, University of Illinois at Urbana Champaign, 104 S. Wright St., Urbana, IL 61801, United States
[b] Mechanical Science & Engineering, University of Illinois at Urbana Champaign, 1206 W. Green St., Urbana, IL 61801, United States

ARTICLE INFO

Article history:
Received 8 November 2013
Received in final revised form 1 September 2014
Available online 16 September 2014

Keywords:
A. Ductility
A. Stress relaxation
B. Constitutive behaviour
B. Elastic-plastic material
C. Mechanical testing

ABSTRACT

The plastic behavior of Hastelloy X subjected to thermo-mechanical loading was investigated in this work, and the phenomenon of dynamic strain aging was studied under isothermal conditions, using digital image correlation (DIC). The material of interest, Hastelloy X a Ni-based superalloy, is widely used in high temperature applications. It was seen that Hastelloy X exhibits serrated plastic flow behavior between temperatures of 300 °C and 700 °C, as a consequence of the dynamic strain aging effect, which, depending on temperature, manifests as type A/B or A and B oscillations on the uniaxial tension stress–strain curve, and is characterized by strain concentration bands propagating along the length of the specimen. The characteristics of Portevin-Le Chatelier (PLC) band internal strain distribution in uniaxial tension experiments were also investigated. The bands themselves were seen to have internal (sub)bands of two or three smaller strain jumps. An analysis of the strain increments induced by these bands was performed and clearly illustrates the inhomogeneous nature of the deformation – both spatially and temporally. In addition to the uniaxial behavior, biaxial stress states were investigated by studying PLC band formation near a notch in a double notched tensile geometry. Similar macroscopic results to the uniaxial case were seen while the strain bands themselves were seen to initiate in the notch region and travel away from the notches.

1. Introduction

The demand for high performance materials for structural applications in extreme environments has driven the development of new materials like superalloys. To allow realization of functional designs such as structural thermal shields for space vehicles or pressure vessels for nuclear reactors using advanced materials, an understanding of their mechanical response is needed. In the case of metallic materials, it is of particular interest to study their behavior in the plastic regime, and uncover factors causing the observed material response. Many engineering metals exhibit irregular plastic flow, usually manifested as stress serrations (“jerky flow”) or strain jumps (“strain staircase”) in their uniaxial tensile response. Such irregular macroscale plastic flow, observed only in limited regimes of strain rate and temperature and sometimes above a critical strain

* Corresponding author. Tel.: +1 217 333 2242; fax: +1 217 244 0720.
E-mail address: lambros@illinois.edu (J. Lambros).
[1] Present address: Applied Materials Inc., Sunnyvale, CA, United States.
[2] Present address: Intel Corporation, Hillsboro, OR, United States.

http://dx.doi.org/10.1016/j.ijplas.2014.09.001
0749-6419/

(Wagenhofer et al., 1999), is caused by inhomogeneous deformation within various localization bands that can be either static or propagating along a specimen. The Portevin-Le Chatelier (PLC) effect is characterized by such instabilities in plastic flow and strain localizations, attributed primarily to a dynamic strain aging effect in which diffusion of solute atoms and dislocation motion occur over comparable time scales therefore necessitating the dislocations to continuously overcome the obstacles. Several factors, such as temperature and strain rate influence the occurrence of the PLC effect, which is also affected by the possible presence of precipitates (Thevenet et al., 1999; Argon, 2008; Liang et al., 2009). The presence of precipitates can cause rapid plastic flow upon reaching a critical strain energy, thus influencing the strain needed for the onset of a PLC effect. Extensive studies on the PLC effect and dynamic strain aging have been carried out by, among others, Kubin and Estrin (1990), Clausen et al. (2004), Benallal et al. (2006, 2008), Tong and Zhang (2007), Zavattieri et al. (2009) and Feng et al. (2012). The PLC effect has been associated with the relative mobility of dislocations and pinning obstacles in a metal (Cottrell, 1953; McCormick, 1971; van Den Beukel, 1980). For example, Clausen et al. (2004) showed the association between this serrated flow and localized shearing failure of precipitates in aluminum alloys. Corby et al. (2004) and Zhang et al. (2013), explained the PLC effect in Magnesium alloys. Though a complete understanding of the factors affecting the behavior of serrated plastic flow has not been established, the reason for serrated flow in the stress–strain curve has been attributed to negative strain rate sensitivity, which has been observed in different aluminum alloys (McCormick, 1988; Shabadi et al., 2004; Ranc and Wagner, 2005). There has also been an effort to study instabilities as a consequence of Portevin-Le Chatelier effect and Lüders bands in ferritic steels (Nikulin et al., 2010; Wenman and Chard-Tuckey, 2010; Chan et al., 2012; Hallai and Kyriakides, 2013).

Most structural components also possess geometrical features such as holes, corners or gaps that are necessitated by design to accommodate fasteners, joints, or for weight reduction. Under the influence of combined thermal and mechanical loads, such stress concentration sites may become initiation sites of the dynamic strain aging bands (Swaminathan et al., 2014). The local strain fields can be highly inhomogeneous in such biaxial, or in general triaxial, loading situations. The effect of dynamic strain aging in components with geometric features has received far less attention in the literature. Dynamic strain aging in aluminum alloys with stress concentrators has been studied by Benallal et al. (2008) and Tong et al. (2011). Both works presented a qualitative analysis of the PLC band formation in the presence of U-notches and V-notches at room temperature. Additional study in this area is needed to fully characterize the dynamic strain aging effect in conditions other than uniaxial loading.

Hastelloy X was chosen for the present study as a "simple" high-temperature alloy, with well-known behavior under isothermal high temperature mechanical loading (United States. Dept. of Defense, 2002). Hastelloy X is strengthened by solute hardening and its response is affected by dynamic strain aging. However, its plastic behavior is actually quite complex, as the hardening response under certain thermo-mechanical loading cycles was found to be unbounded by the isothermal stress–strain behaviors at the same test temperatures, *i.e.*, when applying one loading–unloading cycle at elevated temperature followed by one loading–unloading cycle at lower temperature the resulting response does not fall between the lower and higher isothermal stress–strain curves (Miner and Castelli, 1992; Swaminathan et al., 2014). In addition, chromium carbide precipitation in many Ni-based alloys can produce dynamic strain aging effects during deformation. Sakthivel et al. (2012) presented the stress–strain curves for Hastelloy X in the temperature range of 300–1023 K, at three different strain rates. They observed serrated flow at temperatures between 523 K and 927 K. Similar results were seen in Mo et al. (2013) for Ni-based superalloy 617 and Gao et al. (2013) for Ni–Co superalloy TMW.

The main objective of this work is to investigate the PLC effect that is present during plastic deformation of Hastelloy X using both far-field measurements based on load and displacement and near-field measurements using two-dimensional, *i.e.*, single camera, digital image correlation (DIC), and to do so for both homogeneous and nonhomogeneous stress states. Uniaxial tension samples were used for studying nominally uniaxial stress states, and double notched specimens were used to induce a bi-axial stress concentration in order to investigate PLC band formation under multi-axial stress states. The DIC technique allows greater understanding of dynamic strain aging effects as it can provide a wealth of information (*e.g.*, Tong and Zhang (2007) and Renard et al. (2010)), and has not been used at all in the observation of the phenomenon at high temperatures as is done here. More information about DIC, which uses digital images taken before and after deformation to extract in-plane displacement and strain on the sample's surface, can be found in Sutton et al. (2009). From an experimental point of view characterizing dynamic strain aging and PLC band morphology and behavior (Tong and Zhang, 2007) is made possible with DIC, at multiple scales and with suitable spatio-temporal resolution. It may then be possible to understand the micromechanical behavior that affects the continuum scale response of a material that exhibits a PLC effect (Tong, 2005; Abuzaid et al., 2012). Using DIC it is also possible to determine the behavior in extreme environments where other optical techniques may be limited due to complex experimental setups or experimental conditions. This work discusses the response of Hastelloy X at various test temperatures, extends the PLC band formation visualization to temperatures up to 700 °C, and offers an explanation on the interaction between the load history and strain behavior. It also provides some insight on the PLC behavior of Hastelloy across a range of temperatures in the plastic regime.

2. Experimental methods

2.1. Material and sample preparation

The material used in this study is Hastelloy X which is a solution heat treated Nickel-based superalloy with superior strength and oxidation resistance up to 1100 °C, making it a material of choice for combustion zone components in aircraft

and heat shield components in space vehicles (Abotula et al., 2011). The material was obtained from Haynes Corp. and has a chemical composition, as provided by the supplier listed in Table 1. All experiments in this study were conducted using specimens obtained from the same batch (batch heat number: 2600-1-4793), and the specimens were cut in the rolling direction of the plate so as not to include an influence of possible material anisotropy. Monotonic uniaxial tension loading experiments were carried out with the dog-bone specimen shown in Fig. 1(a). The specimens were machined using electro-discharge machining from a stock 3 mm thick plate which was cut in half in the through thickness direction, to produce samples that were 1.5 mm thick. The specimen surface was polished with coarse grit, followed by fine grit, polishing papers to ensure a flat surface for spraying a suitable speckle pattern for use with DIC. Machined double notch specimens, as shown in Fig. 1(b), were also used to carry out the biaxial stress state experiments while imaging the deformation between the two notches. This geometry was used to introduce an in-plane biaxial stress state near the notches, while maintaining the same far-field uniaxial loading conditions. As in the previous case, monotonic loading experiments were conducted at several temperatures, either under isothermal conditions or with temperature jumps.

2.2. Experimental setup

An Instron 8800 servo-hydraulic load frame was used to load the specimens. Loading was controlled by a computer using a LABVIEW interface thus allowing different loading ramp type, as well as load magnitude and loading rate, to be set. For experiments at elevated temperatures, an induction coil connected to a LEPEL induction heater was placed around the specimen. Eddy currents setup in the specimen because of the electric field around the coils heated the specimen. The induction heater current was set to a constant value once the required specimen temperature was achieved. Fig. 1(c) shows the use of an induction coil to heat a uniaxial tension specimen to a test temperature of about 750 °C. Note the intense sample glowing. The specimen surface temperature was measured by welding a K-type (chromel–alumel) thermocouple to the unprepared surface of the specimen, on the opposite side of the area that would be imaged. The thermocouple was connected to a Micristar temperature measurement control and output interface. Experiments with multiple thermocouples along the sample length and width were first carried out to ensure uniformity (±5 °C at peak of 600 °C) of the temperature within the specimen. In subsequent experiments only one thermocouple was used for temperature control purposes, while the induction coils were not disturbed form their position (see Table 2 for a list of samples tested).

For the DIC portion of the experiments, the imaging setup consisted of an IMITech CCD camera (16 frames per second, monochrome) attached to a Navitar 12× zoom lens with a 2× adapter. The 8-bit camera consisted of a 1920 × 1200 pixel CCD array, and was controlled through an I-1394 rewire I/O interface. The assembly was mounted on a tripod with a dual-direction translation stage to allow for focusing on the area of interest of the specimen – especially important for the double notch experiments. Using calibration targets, the field of view was measured to be 4.5 mm × 3 mm at a spatial resolution of 3.4 μm/pixel. The induction heater coils obscure portions of the specimen (see Fig. 1(c)), so imaging had to be done at a location between coils. Here the area of interest (4.5 mm × 3 mm) was chosen such that it was located at the center of the specimen.

Imaging and loading during the experiments were performed using a custom LABVIEW code that allowed simultaneous control of the camera and load frame, as well as continuous data acquisition from the load cell (cross-head load) and actuator LVDT from the load frame. The code allowed data acquisition at a constant frequency selected prior to the start of the experiment. Loading was carried out in displacement control (with a nominal applied strain rate of 10^{-4} s^{-1} for all experiments) and unloading was carried out in load control. Applied load from the load cell and cross-head displacement from the load frame were recorded by the interface every 50 ms. Images were acquired from the LABVIEW-controlled firewire camera every 2 s. Once an experiment was completed, the images were transferred to a commercial image correlation software VIC-2D (Correlated Solutions Inc.). The DIC algorithm measures the cumulative displacement and strain components over the entire area of interest, and uses interpolation for sub-pixel resolution. An initial guess was specified in the reference image for initiating the algorithm, and a subset size of 51 × 51 pixels with an offset of 5 pixels was used to carry out the correlations. This subset size and offset were selected after conducting baseline (*i.e.*, no deformation) and rigid body motion experiments to determine the suitability of the speckle pattern (see next section). In the interest of brevity details of the DIC technique will not be provided here and the reader is referred to Sutton et al. (2009) for more details. In the next section only the specific modifications made in this work to apply DIC to elevated temperatures will be discussed.

Table 1
Composition (in wt.%) of the Hastelloy X used in this study, as supplied by Haynes Corp.

Al	B	C	Co	Cr	Cu	Fe	Mn	Mo
0.10	<0.002	0.075	1.69	21.22	0.10	18.97	0.65	8.40
Ni	P	S	Si	Ti	W			
BAL	0.015	<0.002	0.29	<0.01	0.56			

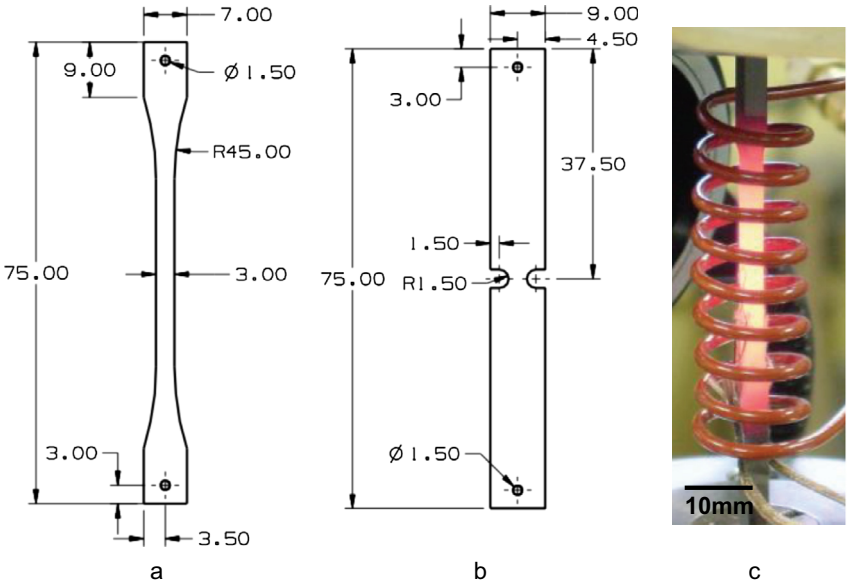

Fig. 1. (a) Dogbone specimen used in the high temperature uniaxial tension tests; (b) double notched specimen used in the high temperature biaxial loading tests; (c) specimen being heated by an induction coil. All dimensions are in mm.

Table 2
Table of uniaxial monotonic tension experiments carried out in this work. Dogbone specimen and double notch specimen geometry are shown in Fig. 1(a) and (b), respectively. Strain rate and applied displacement are far-field measured at the load frame cross head. Loading was done in displacement control, after the specimen reached the specified temperature.

Specimen type	Test temperature (°C)	Strain rate (s^{-1})	Applied displacement (mm)
Dogbone specimen	Room temperature	10^{-4}	3
Dogbone specimen	300	10^{-4}	3
Dogbone specimen	450	10^{-4}	3
Dogbone specimen	500	10^{-4}	3
Dogbone specimen	600	10^{-4}	3
Dogbone specimen	700	10^{-4}	3
Double notch specimen	Room temperature	10^{-4}	.2
Double notch specimen	300	10^{-4}	.2
Double notch specimen	600	10^{-4}	.2

2.3. High temperature DIC measurements

Although not as widespread as room temperature DIC, high temperature DIC has been successfully used in the past by a number of researchers (Turner and Russell, 1990; Lyons et al., 1996; Pan et al., 2010; Swaminathan et al., 2014; Hammer et al., 2014). The DIC technique itself is based on the assumption that there is no change in the intensity values characterizing a surface speckle pattern (either preexisting or user-deposited) before and after deformation. If the pattern is altered for reasons other than deformation, then erroneous measurements could be made. Beyond issues involved in room temperature DIC, two phenomena are of concern as potentially affecting surface pattern quality in high temperature DIC: surface oxidation and sample glowing. In order to prevent oxidation of the prepared specimen surface, a coating of VHT® high temperature white paint was sprayed onto the specimen. The painted surface was then polished with fine grit polishing paper to ensure a smooth and even layer of paint. A random speckle pattern was subsequently sprayed onto the painted surface using an Iwata Custom micron B airbrush. The paint media was VHT® high temperature black paint. In this study the speckle pattern was used with high temperature DIC measurements up to 650 °C so sample glowing was not an issue, although in the past this has been dealt with by performing DIC in the blue light wavelength (*e.g.*, Pan et al., 2010) or more recently with ultraviolet light (Berke and Lambros, 2014)).

Despite glowing not being an issue in the present experiments, preforming high temperature DIC measurements is more complex than their room temperature counterpart. Therefore additional means of improving measurement accuracy were sought. The technique of image averaging (Tong, 2005) was used to investigate whether it is possible to minimize the contribution of random noise on the measured strain fields. Images were acquired at a frame rate of 15 frames per second (fps) for a period of 5 s both at the beginning and end of the loading cycle. (During loading image acquisition rate for all other experiments was 0.5 fps, *i.e.*, one image every 2 s.) The images were then averaged using a MATLAB image processing toolbox and a user-developed code. Image averaging reduced the noise inherent in recording the pixel gray level for a given CCD

camera array. Fig. 2 shows the effect of averaging a series of images on the sensor noise present in the image, by varying the number of images averaged in each case. The image on the left corresponds to a randomly selected single image acquired at room temperature. The middle and right hand images in Fig. 2 show the average of 10 and 25 images recorded in a sequence, respectively. Below each image in the figure is its corresponding intensity count histogram. It can be seen that the histogram of intensity distribution is considerably smoother when averaging is used.

A dogbone specimen was loaded in uniaxial tension at 600 °C and images were recorded throughout the deformation process. Displacements and strains were then obtained through DIC analysis. In addition, images obtained at the start and end of the experiment were used for the image averaging as described above. Fig. 3 shows a line scan perpendicular to the loading direction of the strain component parallel to the loading direction. The results of the two correlations, with and without image averaging, show that there is little difference in the computed strain fields with the averaged result being only slightly below the non-averaged values while exhibiting the same spatial variation along the line scan.

3. PLC behavior under isothermal uniaxial loading conditions

Engineering stress and strain data were computed in two ways: (i) from the far-field load and far-field displacement data, thus providing a purely macroscopic measure of strain, and (ii) from the far-field load but the average strain computed using

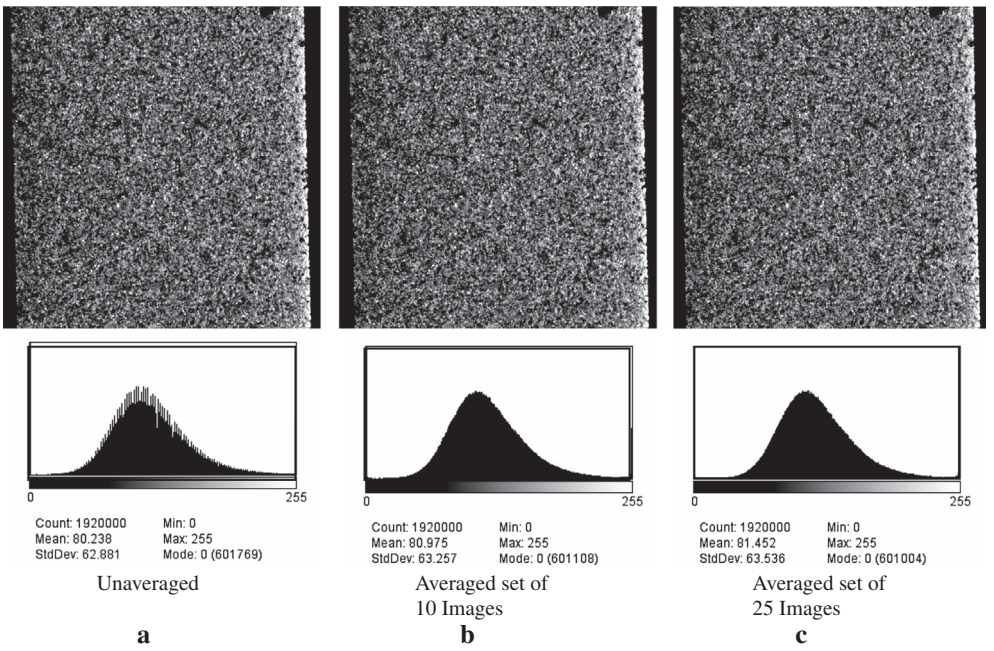

Fig. 2. Noise reduction in digital images by means of image averaging. Averaged images (a) 1, (b) 10, (c) 25.

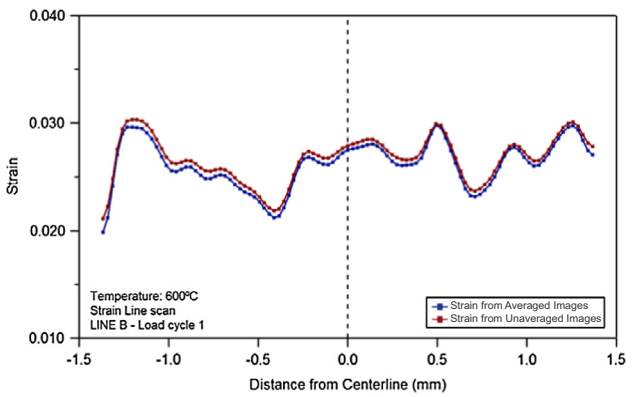

Fig. 3. Engineering strain along a line-scan at the end of load cycle for a high temperature monotonic tension experiment. The profile of strains obtained in the averaged case closely matches the case without averaging. In the averaging process 20 images have been used (specimen: Dogbone).

near-field DIC over the field of view of 4.5 mm × 3 mm for the optical setup used here, thus providing a more local measure of strain. Strains extracted from displacements recorded by the load-frame LVDT were corrected to account for machine compliance (Swaminathan, 2012). The uniaxial tension stress–strain response at different temperatures is shown in Fig. 4. Fig. 5, which is a close-up of the region marked by the box in Fig. 4, shows the variation in serrated flow behavior with increasing temperature. The PLC effect is evident at temperatures above 300 °C in Figs. 4 and 5. It is observed here that the strain level for the onset of the PLC effect remains nearly unchanged across temperatures at a strain level just after the initial yield region in Fig. 4. Similar results were observed by Sakthivel et al. (2012). Recall that the data acquisition time at the macroscale is one point every 50 ms. The stress strain response obtained from the DIC-averaged strain is shown in Fig. 6.

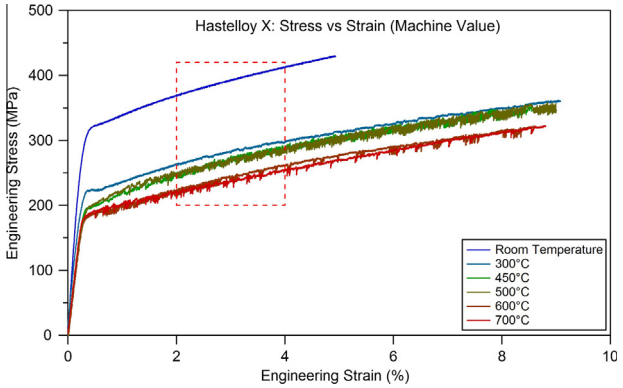

Fig. 4. Stress–strain curves obtained from macroscopic load–displacement data for Hastelloy X. Onset of serrated flow is observed around 300 °C and is seen to reduce at higher temperatures. Close-up of inset red box is shown in Fig. 5 (specimen: Dogbone).

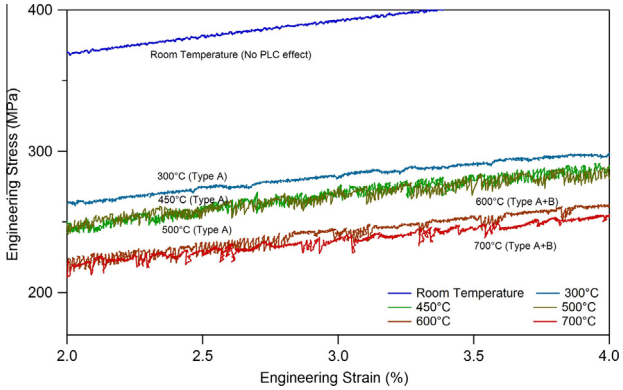

Fig. 5. Close-up of boxed region in Fig. 4 showing serrated flow of Hastelloy X. As temperature increases, there is a transition in the type of serrated flow.

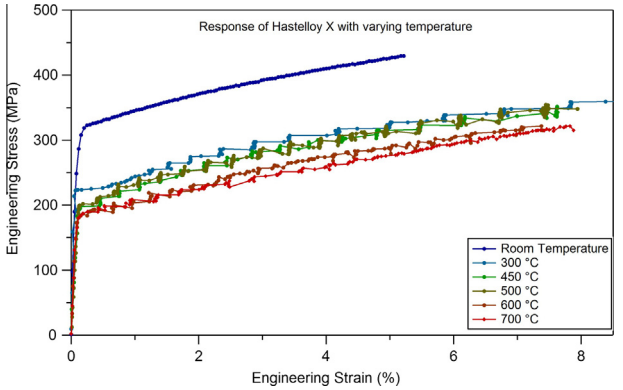

Fig. 6. Stress–strain curves obtained from far field load and local averaged strain measured using DIC (specimen: Dogbone).

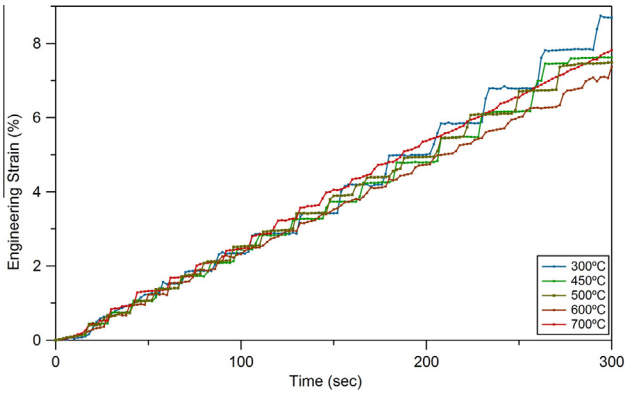

Fig. 7. Strain evolution of Hastelloy X during uniaxial tension at different temperatures. There is evidence of reducing dynamic strain aging at higher temperatures as seen by a decrease in strain jumps (specimen: Dogbone).

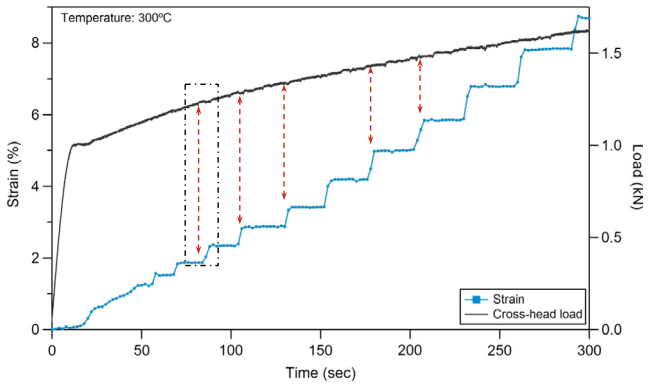

Fig. 8. Strain and load history curves for Hastelloy X at 300 °C. The DIC-recorded strain jumps occur where there are small kinks in the machine load data. The portion of the plot within the box is shown in Fig. 9(a) in greater detail.

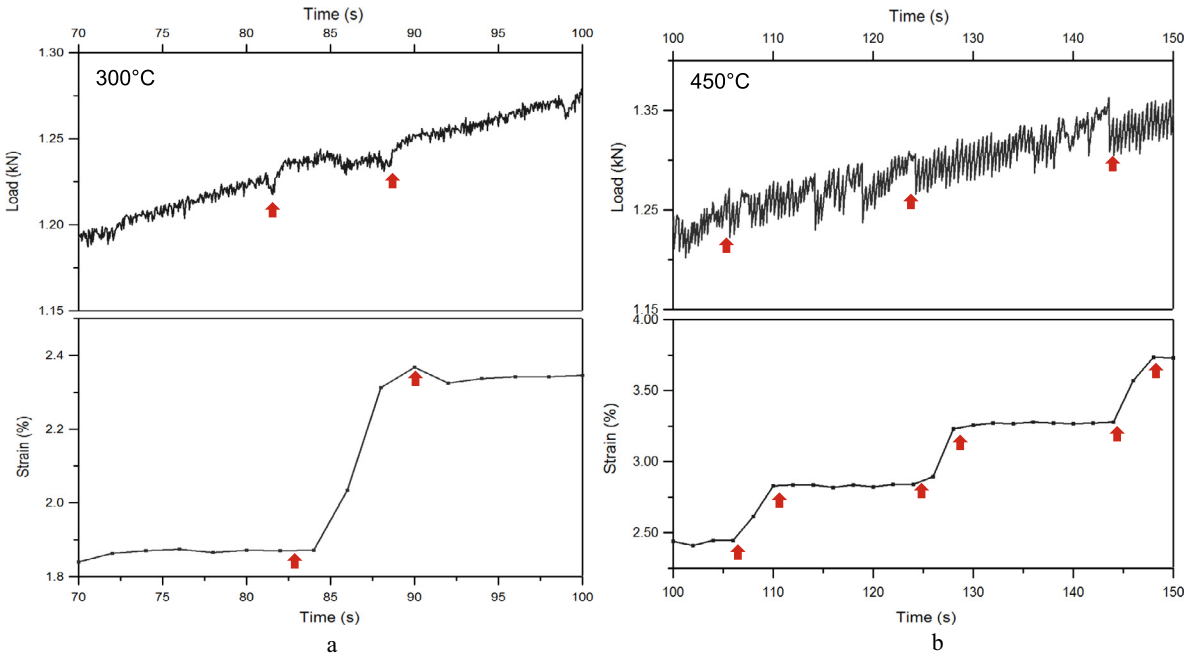

Fig. 9. Loading history and strain evolution showing a change in the loading amplitude, and a corresponding jump in strain, at (a) 300 °C ranging from 70 to 100 s, and (b) 450 °C ranging from 100 to 150 s.

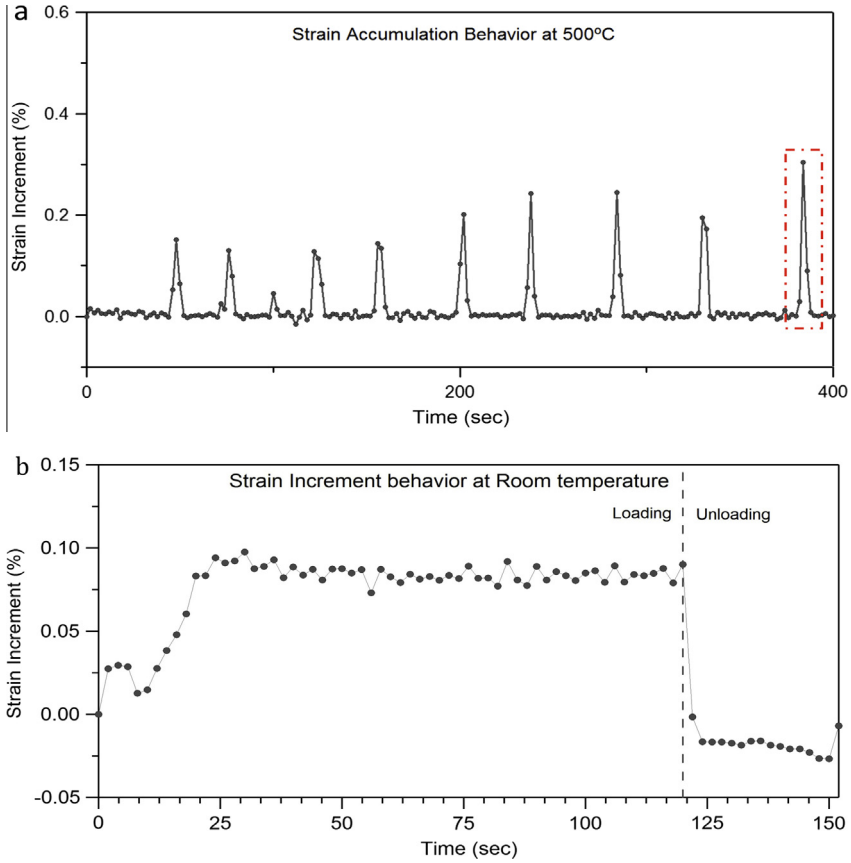

Fig. 10. (a) Mean strain accumulation over time at 500 °C. Discrete peaks are characteristic strain jumps at a particular time period. Certain peaks coincide with bands that can be captured with DIC. The PLC band observed during the period shown in the red box is shown in Fig. 11. (b) Strain increment behavior at room temperature showing constant strain accumulation due to absence of a PLC effect.

In this case jumps appear to be larger, but this is only an artifact because (a) the field of view of the DIC measurement is only a small part of the gauge section, and (b) the data point acquisition time is one point every 0.5 s (rather than every 50 ms as in Fig. 4).

Different types of serrated flow behavior are seen in Fig. 5. The DIC data for the same experiments are shown in Fig. 6. Type A flow is seen to have continuous serrations of the same amplitude, with the stress oscillating about the mean stress. It does not disappear at large strains. The stress–strain curve shows periodic hardening in the form of localized kinks that are followed by a strain relaxation after a jump. Type B flow shows serrations of smaller amplitude than those of type A, but have large drops that occur occasionally. This type of flow usually exists at lower regimes of plastic strain. The strain jumps in this case correspond to the larger change in stress as the material is loaded. For Hastelloy X, tests in the range of 300 °C–500 °C show serrations of type A which occur at strain intervals. Above 500 °C, there is a transition to type A + B and B, which are characterized by low amplitude serrations in the stress–strain curve.

Though the PLC effect in Hastelloy X has been studied recently by Sakthivel et al. (2012), the ability to capture the PLC effect in Hastelloy X at high temperatures with the technique of DIC is unexplored, and is dealt with in detail in this work. DIC allows a more local analysis of the strain fields, establishing a multiscale approach of evaluating the PLC phenomenon, and capturing localization effects at high temperature. This is necessary as the macroscale response alone does not provide sufficient data that can be used towards the development of material models. The DIC-averaged local strain evolution with time for all the tension experiments corresponding to the far-field data of Fig. 4 is shown in Fig. 7. It can be seen that there are distinct strain jumps recorded over the averaged strain results in the 4.5 mm × 3 mm field of view. These jumps in strain reduce at temperatures above 600 °C leaving an almost linearly increasing strain with time, indicating that the PLC effect in this material diminishes as temperature increase beyond 600 °C. In fact this diminishing can also be seen in the reduced oscillations in the stress–strain curves of Fig. 4. As will be seen below, these strain jumps are associated with passage of strain bands through the DIC field of view and are related to corresponding excursions in load.

Fig. 8 shows the macroscale load history together with the local DIC-averaged strain for a 300 °C experiment and Fig. 9(a) shows a closer view of the portion of Fig. 8 highlighted by the dotted red box. The loading history shows occasional small dips, marked in Fig. 9(a) by arrows, as the loading progresses, and results in a corresponding relaxation of the specimen, fol-

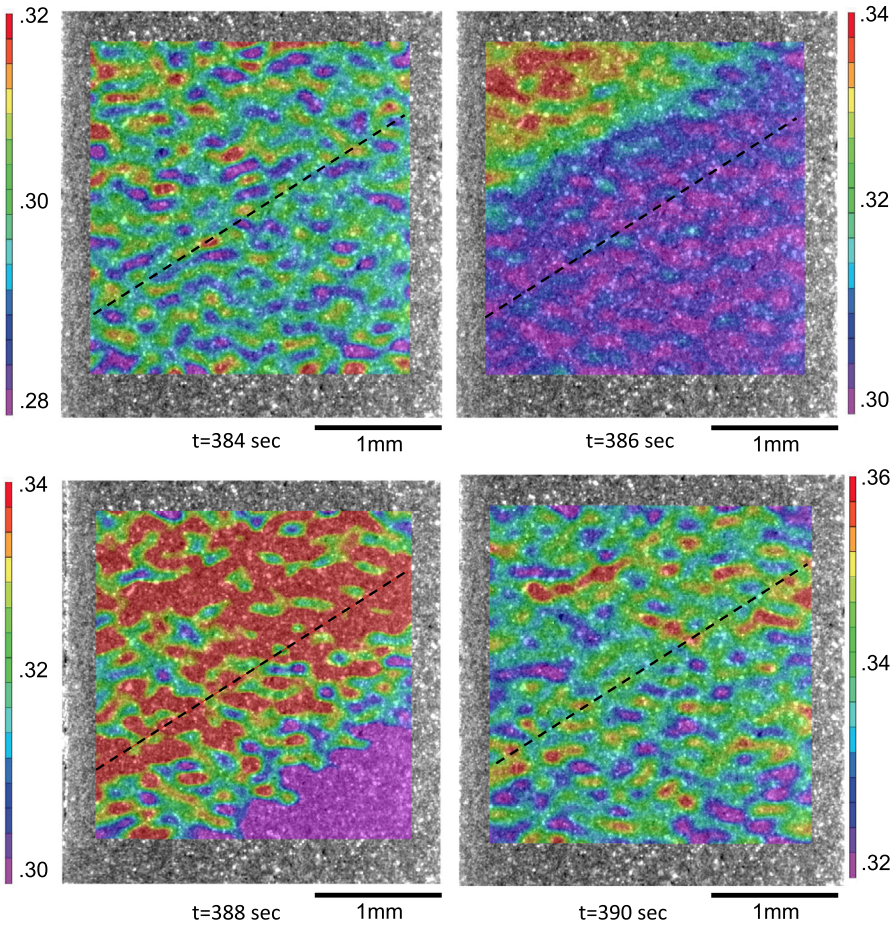

Fig. 11. DIC post-processed images of engineering strain contours showing strain band propagating downward observed at 500 °C. Images captured at 384–390 s at a resolution of 3.60 μm/pixel. The set of images corresponds with the jump in strain denoted by the dashed box in Fig. 10(a).

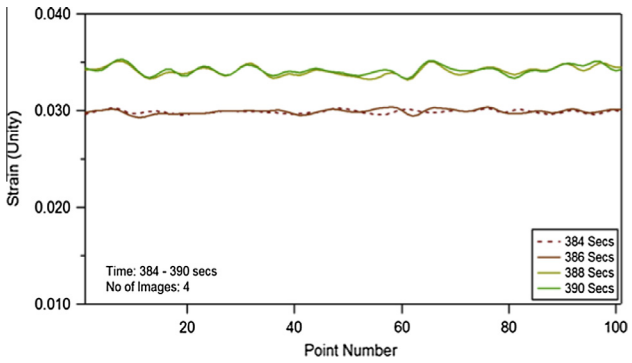

Fig. 12. Axial strain component vs. position along the dashed line shown in the four DIC images in Fig. 11 during uniaxial tension at 500 °C. A strain jump corresponding to the passage of the PLC band at 386 s is seen. There is no further strain accumulation until the next strain jump as seen in the strain increment plot of Fig. 10(a).

lowing a strain jump. Dotted lines marked in Fig. 8 indicate the strain jumps corresponding to the load variations. Fig. 9(a) shows the closer view of a portion of Fig. 8, in the range of 70–100 s and illustrates the relation between the load change and strain jumps more clearly. At 450 °C, a close up of the response for which is shown in Fig. 9(b), the loading exhibits more serrated flow, when compared with the behavior at 300 °C. One possible explanation for this is changing effects of solute drag on the dynamic strain aging processes. In austenitic steels solute drag effects have been seen to originate because of carbon at temperatures around 300 °C. However as temperature increases in the 450–700 °C range, solute drag effects have

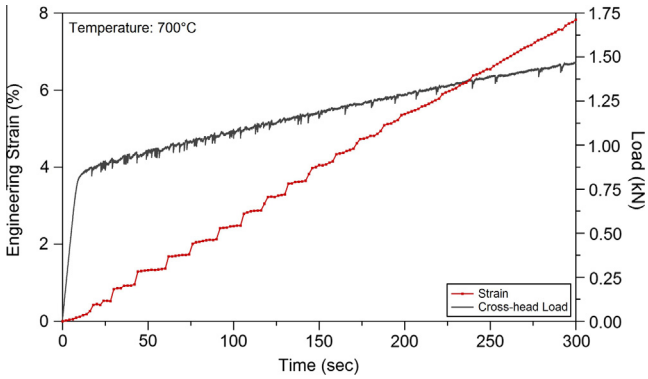

Fig. 13. Strain and load history curves for Hastelloy X at 700 °C. Although initially present, no observable strain jumps are seen as the extent of plastic strain increases beyond 200 s. However, there are periodic load drops even after that time.

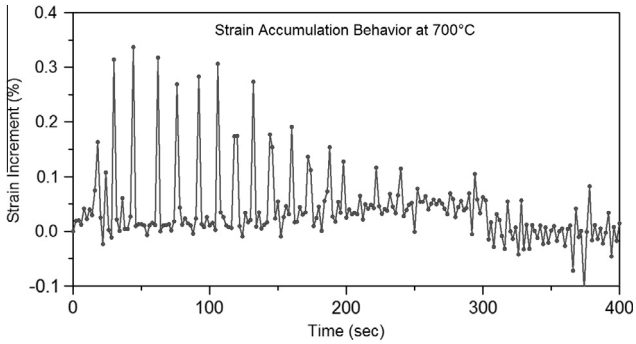

Fig. 14. Mean strain accumulation over time at 700 °C. Strain jumps show decreasing amplitude, eventually showing very small increments that are characteristic of high temperature plastic flow.

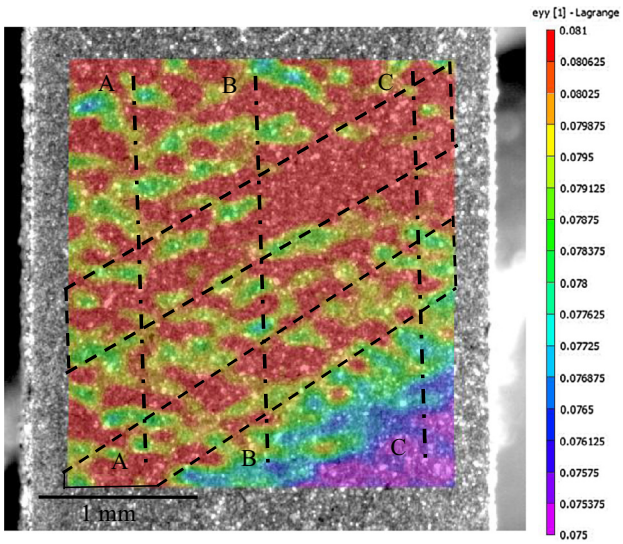

Fig. 15. Full field DIC-measured axial strain showing a PLC band composed of at least two segments. The band is seen propagating diagonally downward. Line scans along A–A, B–B and C–C shows the band morphology (Fig. 16), indicating the strain increase in multiple steps corresponding to the two branches of the band.

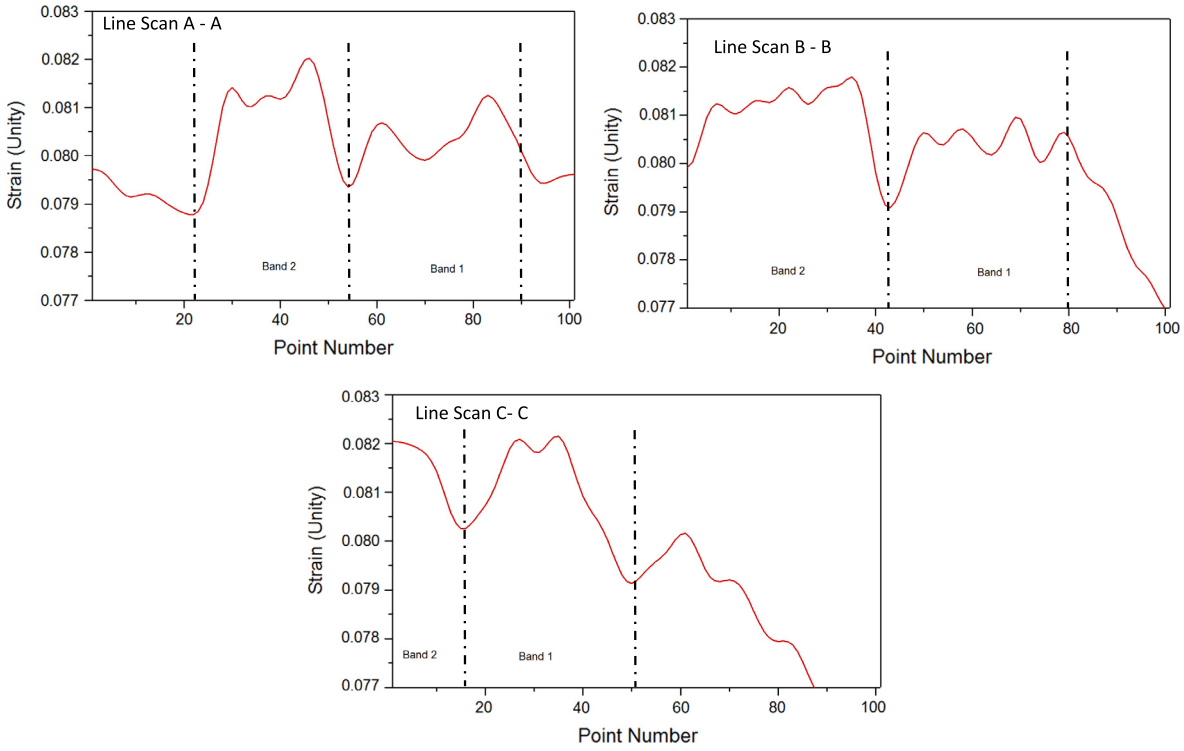

Fig. 16. Line scan of strain along A–A, B–B and C–C (from Fig. 15). The difference between the initial and final strain states is the strain jump caused by the propagation of the PLC band.

been seen to originate primarily from the presence of chromium, thus changing the nature of the oscillations in the stress–strain curve (Jenkins and Smith, 1969). Although we do not have direct evidence of this here, it is possible that the effect of different solute induced drag is what is responsible for the different serration behavior at different temperatures in Hastelloy X as well.

Though it is not always possible to capture the band propagating through the somewhat limited region of DIC observation at the temporal imaging rate used here, it is possible to ascertain whether a band did pass through and result in a strain jump by looking at the increment of DIC-averaged strain. As was mentioned earlier, the induction heater coils obscure a large part of the specimen and the camera system has to be focused onto the sample through a gap in the coils limiting the field of view and hence making it impossible to visualize the band propagating along the entire gage length. The average strain measured by DIC was computed over the region of observation, and the *increment* between mean strains in successive images was calculated and is plotted as a function of time in Fig. 10(a) for the 500 °C case. Unlike the continuous strain accumulation seen during the room temperature experiment (Fig. 10(b)), in the 500 °C experiment, discrete peaks show that strain jumps occur in the region of DIC observation as the applied displacement increases. A trend of greater strain increments is also seen at greater plastic strains. There is a prolonged effect due to dynamic strain hardening with increasing strain, which is seen even at 400 s of testing at strain rates of 10^{-4} s^{-1}.

Since the magnification used here is much higher than that used in Tong and Zhang (2007), the field of view is much smaller. Therefore, only a portion of the band was recorded in our experiments whenever it happened to enter the DIC field of view. One such band is shown in the sequence of four successive DIC images presented in Fig. 11 which correspond to the load jump highlighted by the dashed rectangle in Fig. 10(a). A clear region of lower strain is seen, along with an angled band, which causes an increase in the local strain as it propagates through the specimen (Zavattieri et al., 2009). At time t = 382 s (t = 0 s corresponds to the beginning of loading) the strain field is fairly uniform and averages to the far-field value. At 386 s, *i.e.*, the immediately successive frame acquired, a part of the inclined strain concentration band appears in the upper left portion of the imaged area. In the next frame at t = 388 s, the inclined band has traveled downwards and has enveloped most of the image. Finally, at t = 390 s, the band has left the area of observation and a uniform strain field is again established but at a higher strain level.

A line scan of the vertical (axial) strain for the four different time instances along the dashed line illustrated in Fig. 11, and running parallel to the band at an inclination of 28°, is shown in Fig. 12. Both at 384 s and 386 s, the strain level is around 0.03 and corresponds well to the far-field nominal strain at that time instant measured by the load frame. Although the strain is expected to uniformly increase with time when the loading is homogenous, Fig. 12 shows a jump in strain between 386 s and 388 s, and then a stabilization of strain at the new level. This confirms that the passage of the band seen in Fig. 11 is

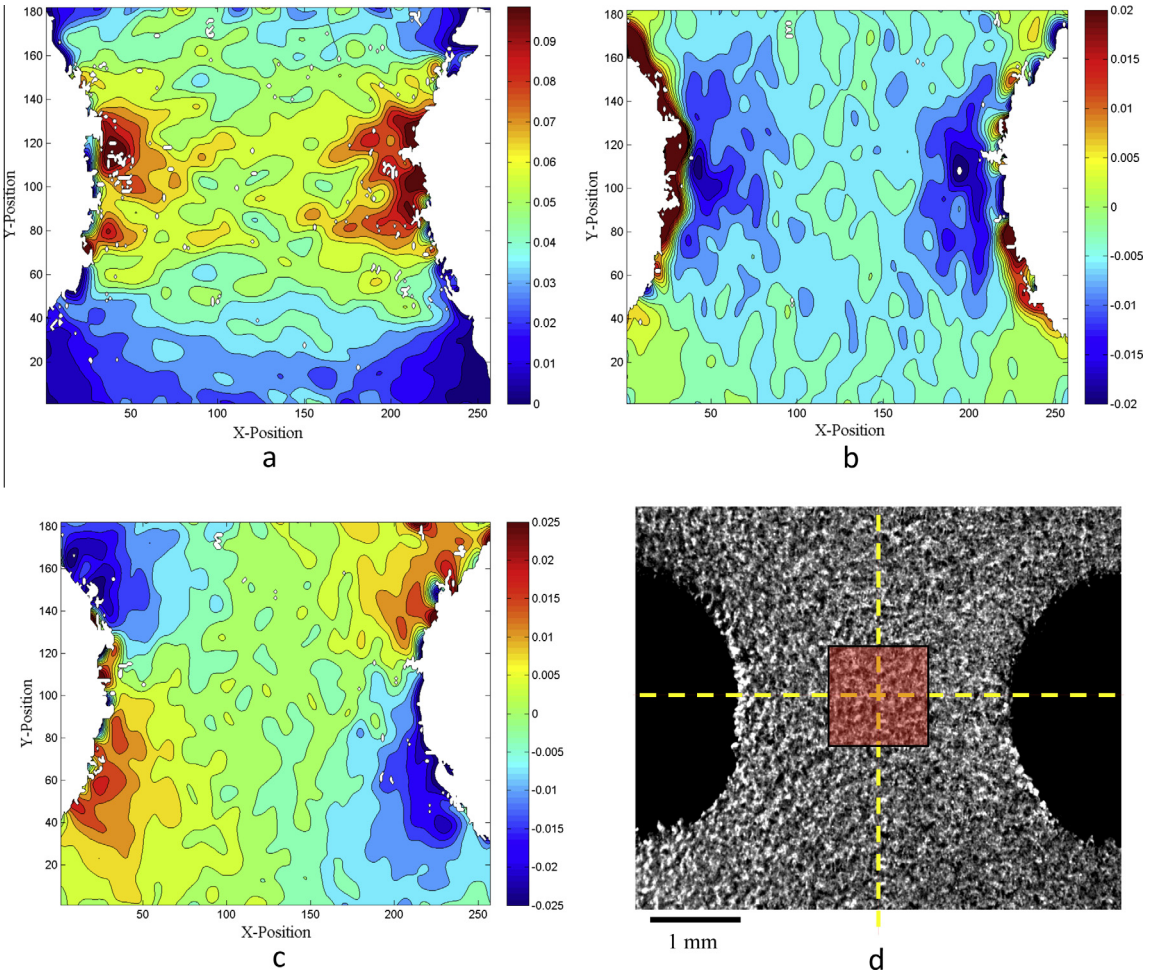

Fig. 17. (a) Vertical strain (ε_{yy}) obtained from DIC analysis indicating an inhomogeneous strain field with stress concentration near the notch tip, (b) transverse strain (ε_{xx}), (c) shear strain (ε_{xy}) and (d) specimen with speckle pattern and the window over which strain evolution is averaged.

associated with an increase in strain increment, as was seen in the average strain increment measurements of Fig. 10(a). The dynamic straining behavior described here is observed to be similar in the 300–500 °C range and also agrees with the macroscale observations of Sakthivel et al. (2012).

As temperature increases further there is a transition from the A type to A + B type of serrations at temperatures above 500 °C. There is no observable trend in the strain increment, and in fact it is found to diminish at higher strains (after 300 s of loading), as the PLC effect disappears. At 700 °C, there is diminishing A + B type of serrations with increasing strain. On the strain–time curve for 700 °C (Fig. 13), the serrations are more widely spaced, and do not show continuous serrated flow after 3% strain. This is consistent with previous findings (Miner and Castelli, 1992; Sakthivel et al., 2012) that show the PLC effect in Hastelloy X disappearing at temperatures around 900 K (630 °C). There is material relaxation at periodic intervals, characterized by load drops, but material flow resumes immediately. The strain jumps are much smaller in magnitude than at other test temperatures and no strain jumps are observed after a certain plastic strain level is reached. The mean strain accumulation behavior at 700 °C (Fig. 14) also exhibits reduced strain accumulation that is approaching closer to the behavior at room temperature (compare Fig. 14 to Fig. 10(a) and (b)). After 4% strain (200 s), there is a large drop in the strain peaks, and this corresponds to the nearly linear strain evolution behavior.

4. PLC band morphology

The PLC band itself consists of a high strain front, propagating at an angle between 55–65° to the loading axis. The bands are usually about 0.1–0.2% higher than the mean strain previously calculated over the same area. Fig. 15 shows the DIC-measured profile of a strain band at 500 °C seen at t = 242 s (see Fig. 10(a)). Unlike the observations of Tong and Zhang (2007), the band is highly non-homogenous and is actually comprised of multiple bands that propagate together. When viewed at the

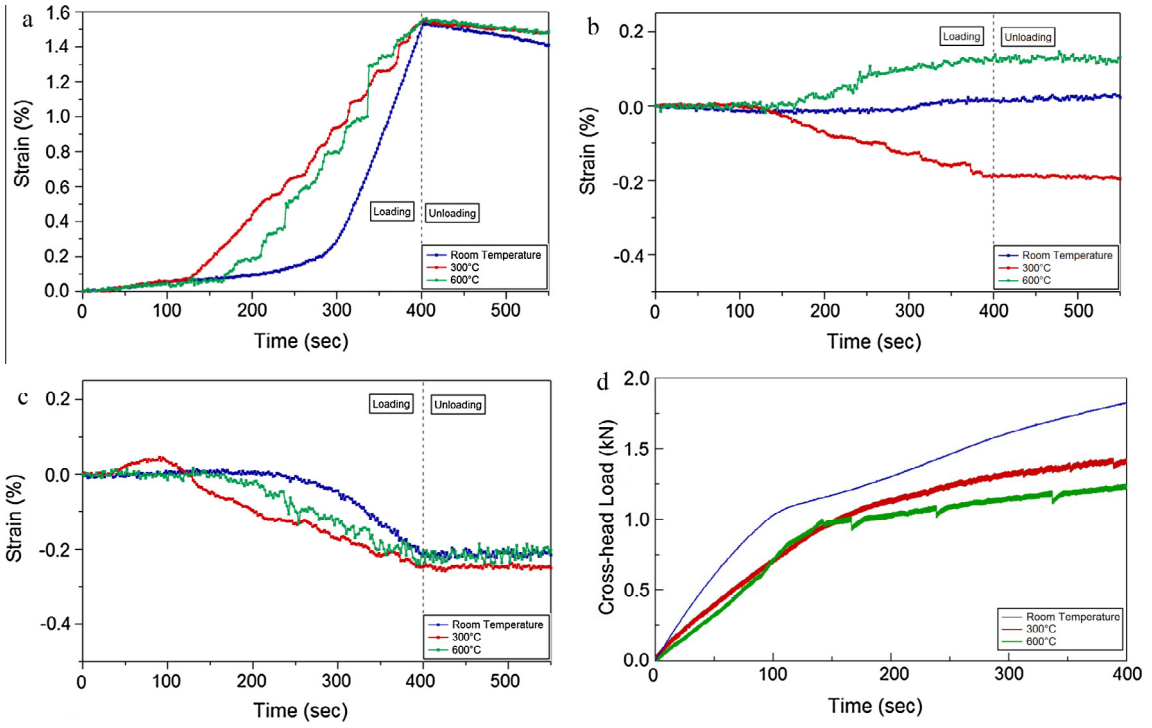

Fig. 18. Strain history at different temperatures under the influence of the notch. There is evidence of dynamic strain aging at 300 °C and 600 °C. (a) Axial strain along loading direction, (b) shear strain, (c) transverse strain and (d) loading history showing load drops at higher temperatures.

length scale used in this work, the band exhibits a gradual increase along the front, reaching a maximum, and then reducing to a far-field value that is greater than the strain prior to the passage of the band. It can be seen that the band is highly branched, suggesting a possible dependence on local microstructure.

Fig. 15 shows that the strain band is made of multiple segments propagating together through the region of the specimen under observation. In this case the strain field shows two band segments that propagate together at the same velocity. Each segment contributes to a strain increment, and there is relaxation (most likely unloading of a part of the elastic strains) after each segment of the band passes through. There is also a gradual increase in strain between the segments. Multiple vertical line scans of the specimen strain along the band in the direction of the propagation, plotted in Fig. 16 along lines A–A, B–B and C–C of Fig. 15, reveal a large contribution of the first segment passing through the region, followed by smaller increments as the successive segments travel through. Since the total band is inclined, certain areas of the field of view along the same horizontal line show greater strain, as the band propagates. The scan along A–A shows that the band has passed through completely, whereas C–C shows the second branch contributing to the strain.

5. PLC behavior under isothermal biaxial loading conditions

Using DIC allows us to study the localized plastic strain evolution in the vicinity of a notch where biaxial conditions will be present. This will shed light into the evolution of the PLC effect in the presence of stress concentrators as was studied for the room temperature response of an aluminum alloy in Tong et al. (2011). By conducting similar experiments to those described above, but using the double notch geometry shown in Fig. 1(b) we can obtain a full field measure of strain in the region around the notches. Fig. 17(a)–(c) shows the measured full field strain along the axial direction (direction of loading), the in-plane shear component and the transverse component, respectively, of a monotonic tension experiment at 600 °C. As expected, there is a strain concentration at each notch tip, which decreases as the center of the specimen between the two notches is approached. The strain fields are generally symmetric, but show small variations locally in the DIC measurement. This can be attributed to a combination of underlying grain structure and the presence of the notch. Thus, the average strain in a small region between the two notches, highlighted as the red[3] area in Fig. 17(d), was computed in order to study strain history evolution. The region is selected such that it is centered about both the loading and notch axes. Fig. 18(a) shows the spatially averaged axial (loading direction) strain history in this region for different temperatures. The corresponding

[3] For interpretation of color in Fig. 17, the reader is referred to the web version of this article.

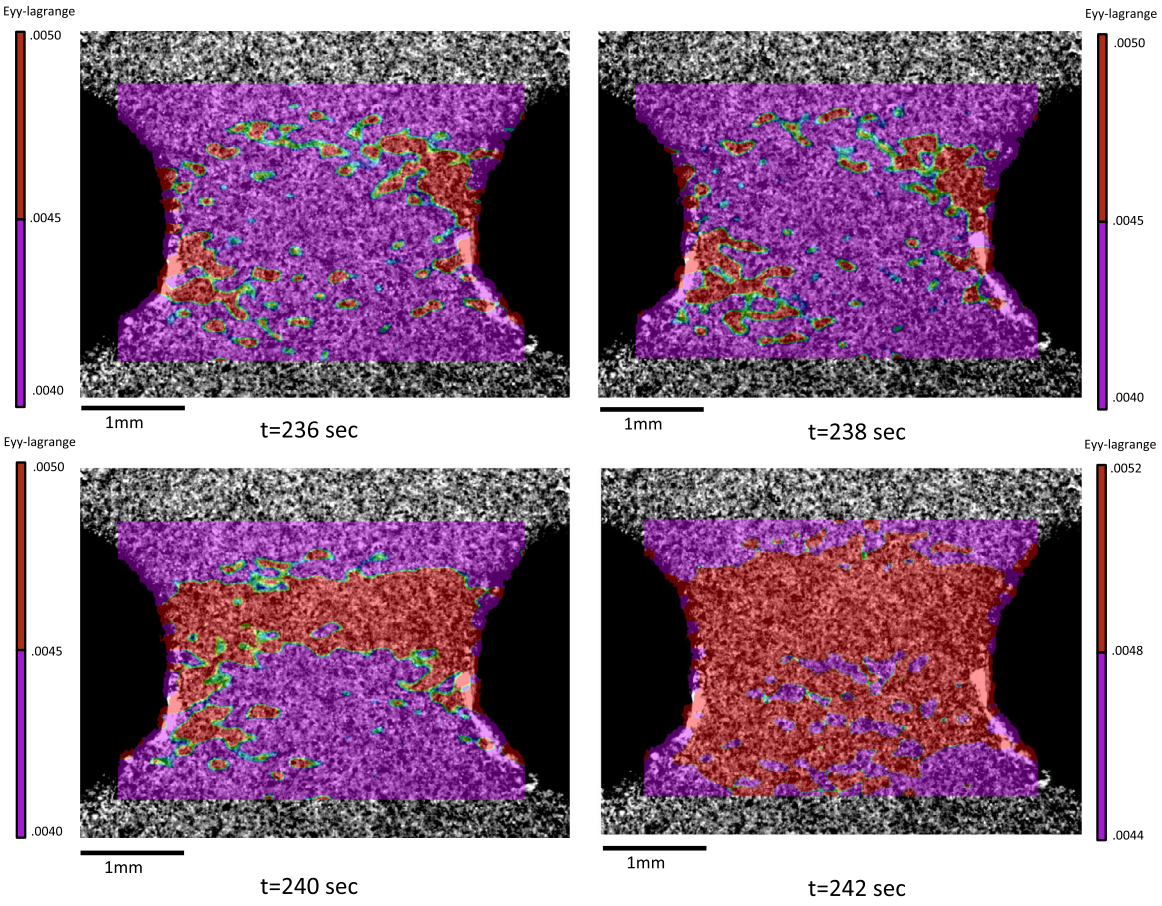

Fig. 19. A half band is seen to originate at the left notch corresponding to the strain jump at 240 s for the 600 °C experiment. The band ceases to propagate beyond the notched section, due to a large area change.

load is shown in Fig. 18(d). At room temperature, the response shows uniform and smooth strain evolution (*i.e.*, no PLC effect present), but at higher temperatures, jumps in strains are evidence of localized serrated plastic flow. At 300 °C, the strain jumps are more continuous, and of lower amplitude than at 600 °C, where the flow is interrupted by large jumps in between smaller strain jumps. Since all experiments were carried out under displacement control (constant strain rate of 10^{-4} s^{-1}), the serrations are a consequence of load drops, which are visible in Fig. 18(d) as the temperature increases. Fig. 18(b) and (c) shows the evolution of the transverse and the shear strain components in the same region shown in Fig. 17(d), which also exhibit some, though less, non-uniform strain accumulation than their axial counterpart in Fig. 18(a).

A closer analysis of the strain evolution shows evidence of serrated flow that is caused as a result of dynamic strain aging. Fig. 19 shows DIC measured strain concentration bands observed originating at the notch root during a 600 °C experiment. The bands propagate either upwards or downwards, away from the notch section, although the specific propagation direction cannot be ascertained from these images. It is seen that the regions of largest strain are not at the area of least cross section, *i.e.*, the area between the notch tips. Instead, the bands originating at an angle to the horizontal axis cause the strain to be concentrated away from the notch tip, and the band has a curved profile. Fig. 19 corresponds to a strain jump observed at 240 s, and a half band is initiated at the notch tip. A half band is seen to originate at each notch tip simultaneously, but with the opposite sense of inclination, *i.e.*, the right band originates at 60° to the loading axis, whereas the left band is seen at −60°. The band propagation is restricted to the notch root due to the large change in cross-sectional area of the specimen. Results from a second jump later on (at 340 s) during the same 600 °C experiment, shown in Fig. 20, illustrates similar, though not identical results. A full band, indicating interaction of both notches, contributes to the localized strain jump. The strain state after propagation of the band is also shown in the sequence of images. The band morphology is similar to the PLC bands observed in the uniaxial tension experiments, with the bands showing localized branching. However, the strain in the bands is much higher in the presence of stress concentrations, causing a jump of 0.2–0.4% (compared to 0.1–0.2% in uniaxial tension experiments without stress concentration), suggesting a connection between the local geometry and the PLC effect.

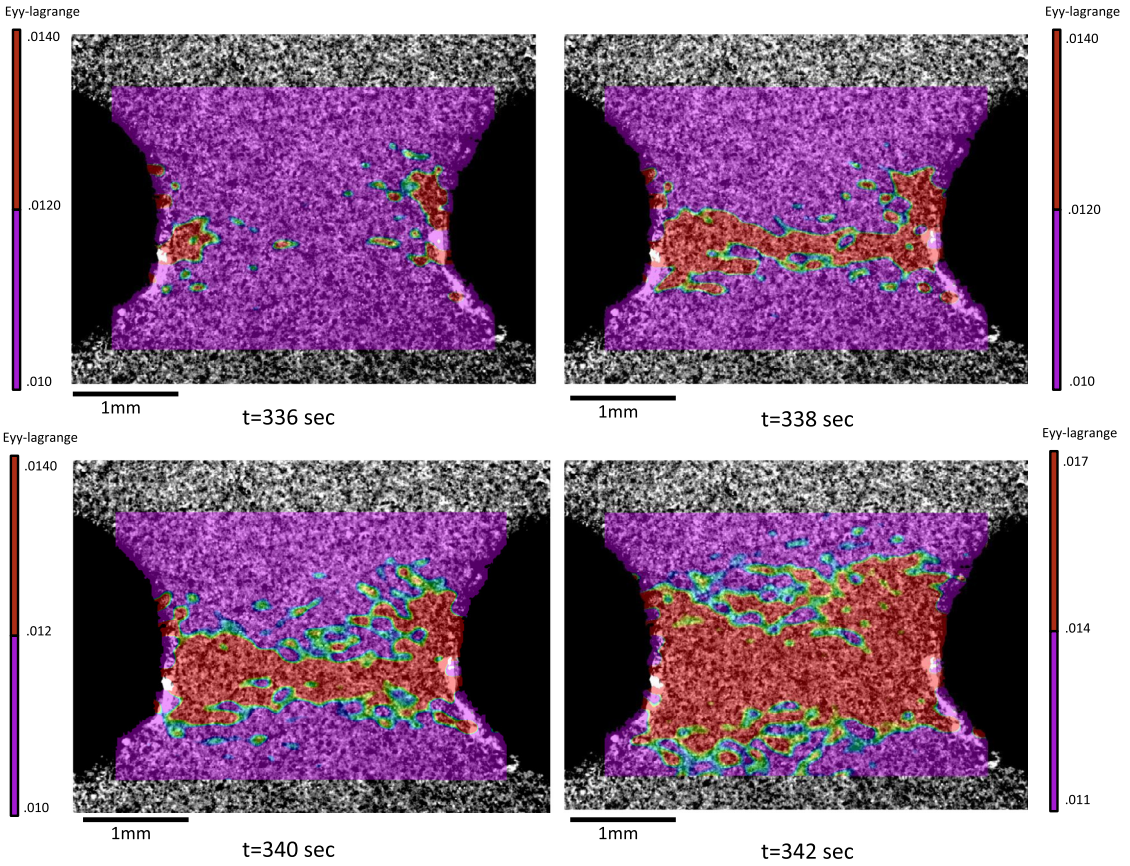

Fig. 20. Progression of a PLC band showing strain accumulation around the notches. The strain fields correspond to 336 s, 338 s, 340 s and 342 s for the 600 °C experiment.

6. Conclusions

Isothermal tension experiments at constant strain rate were conducted to obtain the response of Hastelloy X material at different temperatures. The stress strain curves showed the existence of serrated flow behavior in the temperature range of 300–700 °C. At lower temperatures (300–450 °C), continuous serrations of constant amplitude were observed, whereas at higher temperatures (above 500 °C) regions of small serrations were seen between periodic large jumps in the load. These jumps were associated with strain bands propagating through the specimen, causing local shearing and a jump in strain. Closer observation of the PLC bands revealed that each band comprised of multiple band fronts, each contributing to the strain increase. The effect of dynamic strain aging under a biaxial state of stress was also studied. The PLC bands initiated around a stress concentration causing further jumps in local strain above what the concentrations would produce. This work provides additional insight into how this process occurs in Hastelloy X at elevated temperatures.

The present study has used the technique of digital image correlation (DIC) to study and characterize the dynamic strain aging process in Hastelloy X at temperatures between 300 °C and 700 °C in detail. The strain increment behavior over a small window showed the non-continuous nature of strain increase, with a certain time period of specimen relaxation, that corresponds to the time interval between two bands passing through the same region. The results produced from this study have provided an increased knowledge of the effects of dynamic strain aging on the plastic deformation behavior of Hastelloy X. DIC measurements allowed a link between the macroscale load–displacement or stress–strain response and strain measured over a more local area of the material. They also allowed characterization of the serrated flow behavior over the entire field of view.

Acknowledgements

The authors would like to thank the members of the High Temperature Materials Laboratory at the University of Illinois. In addition interactions with the Midwest Structural Sciences Center at the University of Illinois (sponsored by the Air Force Research Laboratory under Agreement Number FA8650-06-2-3620) are gratefully acknowledged. We are also grateful for partial support provided by AFOSR Award No. FA9550-12-1-0386 (Dr. David Stargel program monitor).

References

Abotula, S., Shukla, A., Chona, R., 2011. Dynamic constitutive behavior of Hastelloy X under thermo-mechanical loads. J. Mater. Sci. 46, 4971–4979. http://dx.doi.org/10.1007/s10853-011-5414-y.

Abuzaid, W.Z., Sangid, M.D., Carroll, J.D., Sehitoglu, H., Lambros, J., 2012. Slip transfer and plastic strain accumulation across grain boundaries in Hastelloy X. J. Mech. Phys. Solids 60, 1201–1220.

Argon, A.S., 2008. Strengthening Mechanisms in Crystal Plasticity. Oxford University Press, Oxford, UK.

Benallal, A., Berstad, T., Børvik, T., Clausen, A.H., Hopperstad, O.S., 2006. Dynamic strain aging and related instabilities: experimental, theoretical and numerical aspects. Eur. J. Mech. – A/Solids 25, 397–424.

Benallal, A., Berstad, T., Børvik, T., Hopperstad, O.S., Koutiri, I., de Codes, R.N., 2008. An experimental and numerical investigation of the behaviour of AA5083 aluminium alloy in presence of the Portevin Le Chatelier effect. Int. J. Plast. 24, 1916–1945.

Berke, R.B., Lambros, J., 2014. Ultraviolet digital image correlation (UV-DIC) for high temperature applications. Rev. Sci. Instrum. 85, 045121. http://dx.doi.org/10.1063/1.4871991.

Chan, C.W., Chan, S.H.J., Man, H.C., Ji, P., 2012. 1-D constitutive model for evolution of stress-induced R-phase and localized Lüders-like stress-induced martensitic transformation of super-elastic NiTi wires. Int. J. Plast. 32–33, 85–105.

Clausen, A.H., Børvik, T., Hopperstad, O.S., Benallal, A., 2004. Flow and fracture characteristics of aluminium alloy AA5083H116 as function of strain rate, temperature and triaxiality. Mater. Sci. Eng.: A 364, 260–272.

Corby, C., Cáceres, C.H., Lukáč, P., 2004. Serrated flow in magnesium alloy AZ91. Mater. Sci. Eng.: A 387–389, 22–24.

Cottrell, A.H., 1953. A note on the Portevin-Le Chatelier effect. Proc. Royal Soc., Philosophical Magazine Series 7, vol. 44, pp. 829–832.

Feng, X., Fischer, G., Zielke, R., Svendsen, B., Tillmann, W., 2012. Investigation of PLC band nucleation in AA5754. Mater. Sci. Eng.: A 539, 205–210.

Gao, Y., Fu, S.H., Cheng, T., Huo, X., Zhang, Q.C., 2013. 3D digital image correlation investigation of PLC effect in a new Ni–Co base superalloy. In: Quan, C., Qian, K., Asundi, A. (Eds.), pp. 87691O–87691O–5.

Hallai, J.F., Kyriakides, S., 2013. Underlying material response for Lüders-like instabilities. Int. J. Plast. 47, 1–12.

Hammer, J.T., Seidt, J.D., Gilat, A., 2014. Strain measurement at temperatures up to 800 °C utilizing digital image correlation. In: Jin, H., Sciammarella, C., Yoshida, S., Lamberti, L. (Eds.), Advancement of Optical Methods in Experimental Mechanics, vol. 3. Springer International Publishing, Cham, pp. 167–170.

Jenkins, C.F., Smith, G.V., 1969. Serrated plastic flow in Austenitic steels. Trans. TMS-AIME 245, 2149.

Kubin, L.P., Estrin, Y., 1990. Evolution of dislocation densities and the critical conditions for the Portevin-Le Châtelier effect. Acta Metall. Mater. 38 (5), 697–708.

Liang, S., Qing-Chuan, Z., Peng-Tao, C., 2009. Influence of solute cloud and precipitates on spatiotemporal characteristics of Portevin-Le Chatelier effect in A2024 aluminum alloys. Chin. Phys. B 18, 3500–3507. http://dx.doi.org/10.1088/1674-1056/18/8/061.

Lyons, J.S., Liu, J., Sutton, M.A., 1996. High-temperature deformation measurements using digital-image correlation. Exp. Mech. 36, 64–70.

McCormick, P.G., 1971. The Portevin-Le Chatelier effect in an Al–Mg–Si alloy. Acta Metall. 19, 463–471.

McCormick, P.G., 1988. Theory of flow localisation due to dynamic strain ageing. Acta Metall. 36, 3061–3067.

Miner, R.V., Castelli, M.G., 1992. Hardening mechanisms in a dynamic strain aging alloy, HASTELLOY X, during isothermal and thermomechanical cyclic deformation. Metall. Trans. A 23, 551–561.

Mo, K., Lovicu, G., Chen, X., Tung, H.M., Hansen, J.B., Stubbins, J.F., 2013. Mechanism of plastic deformation of a Ni-based superalloy for VHTR applications. J. Nucl. Mater. 441 (1–3), 695–703.

Nikulin, I.A., Kaibyshev, R.O., Skorobogatykh, V.N., 2010. Portevin-Le Chatelier effect and strain behavior of austenitic steel 02Kh18N8G2FV2AB at high temperatures. Metal Sci. Heat Treat. 52, 135–139.

Pan, B., Wu, D., Xia, Y., 2010. High-temperature deformation field measurement by combining transient aerodynamic heating simulation system and reliability-guided digital image correlation. Opt. Laser. Eng. 48, 841–848.

Ranc, N., Wagner, D., 2005. Some aspects of PortevinLe Chatelier plastic instabilities investigated by infrared pyrometry. Mater. Sci. Eng.: A 394, 87–95.

Renard, K., Ryelandt, S., Jacques, P.J., 2010. Characterisation of the Portevin-Le Chatelier effect affecting an austenitic TWIP steel based on digital image correlation. Mater. Sci. Eng. A 527, 2969–2977.

Sakthivel, T., Laha, K., Nandagopal, M., Chandravathi, K.S., Parameswaran, P., Panneer Selvi, S., Mathew, M.D., Mannan, S.K., 2012. Effect of temperature and strain rate on serrated flow behaviour of Hastelloy X. Mater. Sci. Eng: A 534, 580–587.

Shabadi, R., Kumar, S., Roven, H.J., Dwarakadasa, E., 2004. Characterisation of PLC band parameters using laser speckle technique. Mater. Sci. Eng: A 364, 140–150.

Sutton, M.A., Orteu, J.J., Schreier, H., 2009. Image Correlation for Shape, Motion and Deformation Measurements: Basic Concepts, Theory and Applications. Springer, New York.

Swaminathan, B., 2012. Thermo-mechanical response and plastic deformation behavior of Hastelloy X at elevated temperatures – role of dynamic strain aging. MS thesis. University of Illinois at Urbana-Champaign.

Swaminathan, B., Lambros, J., Sehitoglu, H., 2014. Digital image correlation study of mechanical response of nickel superalloy Hastelloy X under thermal and mechanical cycling: uniaxial and biaxial stress states. J. Strain Anal. Eng. Des. 49 (4), 233–243.

Thevenet, D., Mliha-Touati, M., Zeghloul, A., 1999. The effect of precipitation on the Portevin-Le Chatelier effect in an Al–Zn–Mg–Cu alloy. Mater. Sci. Eng.: A 266, 175–182. http://dx.doi.org/10.1016/S0921-5093(99)00029-5.

Tong, W., 2005. An evaluation of digital image correlation criteria for strain mapping applications. Strain 41, 167–175.

Tong, W., Zhang, N., 2007. On serrated plastic flow in an AA5052-H32 sheet. J. Eng. Mater. Technol. 129, 332.

Tong, W., Xuan, X., Yao, H., 2011. On the interaction of material heterogeneity and geometric discontinuity in serrated plastic flows. In: 3rd International Conference on Heterogenous Material Mechanics. Shanghai, China, pp. 178–185.

Turner, J.L., Russell, S.S., 1990. Application of digital image analysis to strain measurement at elevated temperature. Strain 26, 55–59.

United States. Dept. of Defense, 2002. Military Handbook – MIL-HDBK-5H: Metallic Materials and Elements for Aerospace Vehicle Structures. U.S. Dept. of Defense, [Washington, D.C].

van Den Beukel, A., 1980. On the mechanism of serrated yielding and dynamic strain ageing. Acta Metall. 28, 965–969.

Wagenhofer, M., Erickson-Natishan, M., Armstrong, R.W., Zerilli, F.J., 1999. Influence of strain rate and grain size on yield and serrated flow in commercial Al–Mg alloy 5086. Scripta Mater. 41, 1177–1184.

Wenman, M.R., Chard-Tuckey, P.R., 2010. Modelling and experimental characterisation of the Lüders strain in complex loaded ferritic steel compact tension specimens. Int. J. Plast. 26, 1013–1028.

Zavattieri, P.D., Savic, V., Hector Jr., L.G., Fekete, J.R., Tong, W., Xuan, Y., 2009. Spatiotemporal characteristics of the Portevin Le Chatelier effect in austenitic steel with twinning induced plasticity. Int. J. Plast. 25, 2298–2330.

Zhang, S.Q., Mao, L., Chen, L.J., 2013. Dynamic strain aging during tensile deformation of extruded AZ81 magnesium alloy. Adv. Mater. Res. 652–654, 1937–1941. http://dx.doi.org/10.4028/www.scientific.net/AMR.652-654.1937.